Coercivity enhancement driven by interfacial magnetic phase separation in SrTiO_{3}(001)/Nd_{0.5}Sr_{0.5}CoO_{3}

M. Sharma, J. Gazquez, M. Varela, J. Schmitt, and C. Leighton

Phys. Rev. B **84**, 024417 — Published 13 July 2011

DOI: 10.1103/PhysRevB.84.024417

Submitted to *Phys. Rev. B.* on 4/11/11

Coercivity enhancement driven by interfacial magnetic phase separation in $SrTiO_3(001)/Nd_{0.5}Sr_{0.5}CoO_3$

M. Sharma[1], J. Gazquez[2,3], M. Varela[3,2], J. Schmitt[1] and C. Leighton[1]*

[1] *Department of Chemical Engineering and Materials Science, University of Minnesota, Minneapolis, MN 55455, USA*

[2] *GFMC, Dept. Fisica Aplicada III, Universidad Complutense de Madrid. Madrid, 28040, Spain*

[3] *Materials Science and Technology Division, Oak Ridge National Laboratory, Oak Ridge, TN 37831, USA*

Thin film perovskite cobaltites have been found to exhibit coercivity values enhanced by almost two orders of magnitude in comparison to bulk. In this work we have investigated this unexplained coercivity enhancement in detail, focusing on epitaxial $SrTiO_3(001)/Nd_{0.5}Sr_{0.5}CoO_3$ films, which display coercivity values up to 40 kOe at low temperatures. Thickness dependent (10–800 Å) magnetometry and magnetotransport studies demonstrate that nanoscopic magnetic phase separation occurs in the interface region of the $Nd_{0.5}Sr_{0.5}CoO_3$ (consistent with recent work on $SrTiO_3(001)/La_{1-x}Sr_xCoO_3$), which is responsible for the degradation in magnetic and electronic properties in the very thin film limit. The coercivity is shown to be intimately related to the existence of this (70Å thick) interfacial phase separated layer, leading us to advance an explanation for the coercivity enhancement in terms of pinning of domain walls by interfacial nanoscopic

ferromagnetic clusters, and a crossover to single domain clusters at very low thickness. Simple estimates of the magnetocrystalline anisotropy (from the maximum coercivity), cluster dimensions (from the superparamagnetic blocking temperature), multi domain to single domain crossover point, and domain wall width, provide quantitative support for this picture.

*Corresponding author: leighton@umn.edu

PACS numbers: 75.47.Lx, 75.70.Cn, 75.60.Jk

I. Introduction

The investigation of complex oxide heterostructures has undergone dramatic expansion in recent years, driven by exciting prospects from both the fundamental and applied perspectives [1]. Much of the scientific interest has focused on the ability to stabilize novel non-equilibrium ground states (either at interfaces, or due to epitaxial strain), or to obtain film properties distinctly different from bulk [1]. Due to the extraordinary functionality of the materials, potential technological applications arise in very diverse areas such as solid oxide fuel cells (SOFCs), catalysis, ferroelectric random access memory (RAM), spintronics, and indeed oxide electronics in general [1]. Given the importance of heterointerfaces in these applications, the well-known issue of degradation in desired properties at interfaces with dissimilar oxides becomes a significant challenge.

Magnetic complex oxides such as the intensively studied perovskite manganites provide a perfect example via two, likely closely related, experimental observations. The first comes from oxide magnetic tunnel junctions (MTJs) such as (001) oriented LSMO/STO/LSMO trilayers (LSMO = $La_{1-x}Sr_xMnO_3$, STO = $SrTiO_3$). In these MTJs the anticipated high conduction electron spin polarization in LSMO, and the close lattice match to STO, lead to exceptionally high tunneling magnetoresistance (TMR) at cryogenic temperatures [2,3]. The TMR decreases rapidly with increasing temperature however (even well below the Curie temperature (T_C)) [2,3], an effect that was linked to the difficulty of maintaining high, thermally stable, magnetization and spin polarization at LSMO surfaces [4] and interfaces [5-8]. The second observation comes from single

ferromagnetic (F) metallic manganite films (e.g. $x \approx 0.3$ LSMO) deposited on single crystal insulating perovskites substrates such as STO(001). Even in this close to ideal situation, degradation in magnetization and conductivity is consistently observed in the very thin film limit [e.g. 9-12], being substantially stronger than what would be expected from conventional finite size effects.

Recently, we investigated this issue of degradation in magnetic and electronic properties in very thin films, using the doped perovskite cobaltite $La_{1-x}Sr_xCoO_3$ (LSCO) as a model system [13]. This is a material that has generated considerable interest from the fundamental magnetism perspective (primarily due to phenomena such as spin-state transitions and magneto-electronic phase separation (MEPS)) [e.g. 14], at the same time being of interest for applications in catalysis [15,16], spintronics, and as electrodes in SOFCs [15,17] and ferroelectric RAM [15,17]. In bulk form this system exhibits the well-known MEPS phenomenon [18]. Nanoscopic hole-rich F clusters form in a semiconducting non-F matrix, as evidenced by a number of techniques, including neutron diffraction [19], Co Nuclear Magnetic Resonance (NMR) [20,21], Small-Angle Neutron Scattering (SANS) [22,23], and inelastic neutron spectroscopy [24,25]. As x is increased the clusters percolate at a critical doping level of $x_c = 0.17$-0.18, inducing a transition to a metallic long-range ordered F ground state [14,22,23]. As x is increased to 0.22 a homogeneous F phase is entered, i.e. the phase-separated regime ends, a fact that can be understood within a doping fluctuation model [23]. T_C eventually approaches room temperature deep in the F phase [14]. Importantly, in the MEPS regime this material was shown to be a natural analog to artificial systems formed by depositing F clusters in a

non-F matrix, leading to an intercluster "GMR-type" effect, directly analogous to intergranular GMR (Giant MagnetoResistance) [22,26]. This intercluster magnetotransport effect thus provides a simple probe of the existence of nanoscopic MEPS, a fact which played a key role in our recent study [13] of the degradation in magnetization and conductivity in $SrTiO_3$(001)/$La_{1-x}Sr_xCoO_3$ films [27,28]. This system was found to enter a suppressed magnetization state below a thickness, t^*, of about 80 Å at $x = 0.5$, coincident with a crossover from metallic-like to insulating-like transport. This crossover was found to be accompanied by the abrupt onset of large, negative, hysteretic, and isotropic MR, which was conclusively demonstrated to be of the intercluster GMR type. This provides strong, albeit indirect evidence that the well-known degradation in electronic and magnetic properties actually occurs due to formation of a thin magnetically phase separated layer near the interface with STO(001), even at compositions that do not exhibit MEPS in bulk. This conclusion was verified via direct detection of the short-range F clusters using SANS [13]. The interface-induced MEPS was then subsequently explained via the observation of subtle depth-wise variations in Sr doping and O content. These variations were ascribed to intrinsic thermodynamic and structural effects, the formation of an O vacancy superstructure to accommodate lattice mismatch with the substrate being the most important [13].

During the course of the STO(001)/LSCO study described above, it was noticed, in agreement with other observations on LSCO [29,30] and LCCO ($La_{1-x}Ca_xCoO_3$) (001) films [31,32], that the coercivity (H_C) is substantially enhanced over the bulk value. This is aptly demonstrated by Fig. 1(b), which displays 10 K hysteresis loops of an $x = 0.5$

LSCO bulk polycrystalline specimen [14], and an 800 Å thick epitaxial film on STO(001) [13]. The bulk H_C is 0.25 kOe, typical for polycrystalline samples of this composition [14,26]. The film H_C on the other hand is 7 kOe, increasing up to 18 kOe at lower thickness. The coercivity is thus enhanced by a factor of almost 100 over the bulk value, the origin of this enhancement being unknown. In terms of executing a systematic study of this H_C enhancement, $Nd_{1-x}Sr_xCoO_3$ (NSCO) is an attractive material due to the fact that, from the currently available data, it exhibits the largest bulk H_C values in the $Ln_{1-x}AE_xCoO_3$ series (*Ln* and *AE* represent lanthanide and alkaline earth ions, respectively) [33-36]. Bulk polycrystalline samples at x = 0.3-0.5 were found to exhibit H_C values of the order of 2-3 kOe (see Fig. 1(a)), which was interpreted by Fondado *et al* [33] in terms of the orbital angular momentum (*L*) contribution of the Nd ions to the magnetocrystalline anisotropy, via the *L*-*S* coupling. The data of Fig. 1(a) demonstrate that this indeed translates into very large H_C values in thin film x = 0.5 NSCO. We find H_C = 27 kOe in the thick film limit (i.e. 800 Å), increasing to almost 40 kOe at lower thickness, as discussed in detail below. We therefore view STO(001)/NSCO as an ideal system in which to study the fundamental physical origins of this extraordinary H_C enhancement.

The object of this work is thus three-fold. We wish to determine; (a) if the STO(001)/NSCO system exhibits the same degradation in magnetic and electronic properties as LSCO(001) in the very thin film limit, (b) if so, whether this degradation can be related to the existence of a nanoscopic magnetically phase separated layer detected via the characteristic intercluster magnetotransport, and (c) whether the observed

H_C enhancement is related in any way to this interface-induced MEPS. As discussed in detail below, the results confirm that the thickness dependence of the magnetic and transport properties is indeed strongly degraded in the very thin film limit, and that this is again related to the existence of interfacial MEPS. Most importantly, the H_C enhancement is found to be intimately related to the formation of this phase-separated layer near the interface with STO(001). The thickness dependence of H_C in fact leads us to advance pinning of domain walls at nanoscopic F clusters in the interface layer, and an eventual crossover to a single domain cluster regime, as the origin of the coercivity enhancement. A simple quantitative analysis of the temperature and thickness dependent magnetometry data demonstrates self-consistency of this picture, providing further support for the model. The results thus provide a complete explanation for the very large H_C values found in thin perovskite cobaltite films, further emphasizing the importance of subtle interfacial phenomena for the magnetic properties of these complex oxide films.

II. Experimental Considerations

NSCO films (x = 0.5 in all cases) were deposited on $SrTiO_3$(001) substrates by reactive sputtering from 2" sintered ceramic targets prepared by conventional solid state reaction [14]. Depositions were performed at a substrate temperature of 700 °C, a deposition rate of 1.8 Å/min (100 W of power), and O_2 and Ar partial pressures of 20 and 50 mTorr, respectively. The base pressure of the system was 1 x 10^{-8} Torr. Post-deposition annealing for 2 hours in flowing O_2 at 500 °C removed all trace of a CoO impurity phase from the x-ray diffraction patterns. Note that these conditions are very similar to those used for the STO(001)/LSCO system studied previously [13], and that

details on optimization of those growth conditions are provided in ref. 37. Structural characterization by high resolution x-ray diffraction (including wide-angle diffraction, rocking curves, in-plane diffraction, and grazing incidence reflectivity) was performed using CuK_α radiation on a Panalytical X'pert system. Thickness and deposition rate determinations were done with x-ray reflectivity. Scanning transmission electron microscopy (STEM) observations were carried out in a VG Microscopes HB501UX dedicated STEM operated at 100 kV. This column is equipped with a Nion aberration corrector and a Gatan Enfina electron energy loss (EELS) spectrometer. Co $L_{2,3}$ and Ti $L_{2,3}$ depth profiles were generated by integrating the intensities under the EELS edges after background subtraction (using a power law fit). The chemical profiles were averaged laterally over approximately 20 nm in the direction parallel to the interface. Specimens for STEM were prepared by conventional methods, i.e. grinding, dimpling, and Ar ion milling. Magnetometry measurements (10 – 300 K, fields up to 70 kOe) were performed in a Quantum Design SQUID system, while magnetotransport (5 – 300 K, fields up to 90 kOe) was measured in a home-built system. We employed soldered In and sputtered Mg/Au contacts in a van der Pauw configuration, using 13.7 Hz ac excitation. All magnetic fields were applied in the plane of the film; all samples had in-plane magnetic anisotropy.

III. Results and Discussion

A high-resolution wide-angle specular x-ray diffraction pattern from a 420 Å thick $x = 0.5$ NSCO film grown on STO(001) is shown in the main panel of Fig. 2(a). The data confirm epitaxy in the direction perpendicular to the substrate, only the diffraction

lines from the (00*l*) family of NSCO planes being present. As discussed in more detail below, the out-of-plane lattice parameter (*c*), wide angle diffraction peak width, and (002) rocking curve width have all been analyzed as a function of thickness (*t*). As shown in the inset to Fig. 2(a), grazing incidence in-plane x-ray diffraction data (i.e. ϕ scans), demonstrate in-plane epitaxy. Comparisons to substrate scans (not shown) confirm the expected "cube-on-cube" epitaxial relationship. Fig. 2(b) shows an expanded view of the wide-angle diffraction data in the vicinity of the NSCO and STO (002) reflection for representative films with thicknesses from 45 to 800 Å. Films with $t < 100$ Å have the (002) reflection at essentially identical diffraction angles (rightmost dotted vertical line in the figure), corresponding to $c \approx 3.730$ Å. Reciprocal space maps around the (013) reflection reveal that the films in this *t* range have in-plane lattice parameters very close to 3.905 Å, meaning that they are fully strained, i.e. pseudomorphic with the STO(001) substrate. The bulk pseudocubic lattice parameter of $x = 0.5$ NSCO (the true structure is orthorhombic with space group *Pnma*) is approximately 3.81 Å [34,36,38], meaning that these films are subject to a 2.43 % biaxial tensile strain in the plane, leading to a *c*-axis lattice parameter considerably smaller than bulk, and subsequently a tetragonal structure. As shown in Fig. 2(b), the situation is distinctly different for films with $t > 100$ Å, the (002) reflection appearing at progressively lower diffraction angles with increasing *t*. This reflects the expected tendency to strain relaxation above some critical thickness (t_{crit}), which is apparently 100 Å in this case (see below for more details). The leftmost vertical dotted line indicates the expected diffraction angle for a fully relaxed film, highlighting that even at 800 Å these films do not fully relax to the bulk lattice parameter. It is worth noting that the t_{crit} we observe here for STO(001)/NSCO (i.e. 100 Å) is a

factor of two smaller than that seen for STO(001)/LSCO at the same x value and deposition conditions [37]. This is qualitatively consistent with the increased lattice mismatch (2.43 %) cf. the LSCO case (1.92 %).

Additional data on the strain relaxation process is shown in Fig. 3, which plots the t dependence of c, the (002) rocking curve full-width at half-maximum, and the length scale Λ, extracted from from the width of the (002) wide-angle diffraction peak using Scherrer's equation. As discussed previously for STO(001)/LSCO [37], these three quantities clearly reveal t_{crit}, which is indicated by the vertical dotted line at t = 100 Å. The c-axis lattice parameter (Fig. 3(a)) is approximately constant for $t < t_{crit}$, relaxing rapidly at higher thickness. This relaxation is also seen in the (002) rocking curve width (Fig. 3(b)), due to the increased mosaicity associated with the strain relaxation mechanism [37]. In STO(001)/LSCO this was directly related to a crossover from a 2D-like to 3D growth mode. This strain relaxation is also evident in the $\Lambda(t)$ data, which deviate downwards from $\Lambda = t$ at 100 Å. This occurs due to the fact that below t_{crit} the out-of-plane diffraction peak width is dominated by finite size effects (the thickness in this case as the scattering vector is purely out of plane), with no contribution from microstrain as the film is uniformly strained throughout its depth. Above t_{crit} however, $\Lambda(t)$ deviates below $\Lambda = t$ due to the microstrain contribution to the peak width which necessarily occurs in partially relaxed films [37].

Further characterization of the structure of these epitaxial STO(001)/NSCO films is provided by the Z-contrast STEM imaging shown in Fig. 4. Fig. 4(a) displays a low

magnification image of a 90 Å-thick film, demonstrating that the film is relatively smooth, and continuous, over long lateral length scales (≈ 2500 Å). The higher magnification image of the interior of a 330 Å thick sample (Fig. 4(b)) reveals the oxygen vacancy superstructure discovered previously in LSCO films [39], which leads to intensity modulation of alternate CoO_2 planes. The formation of this tetragonal superstructure is confirmed by the fast Fourier transform shown in the inset to Fig. 4(b), which displays weaker features midway between the strong primary diffraction spots. Progressively higher magnification microscopy (Figs. 4(c,d)) reveals a sharp coherent interface in atomic resolution images. The extent to which the STO/NSCO interface is chemically abrupt is better assessed in Fig. 4(e) which plots the normalized and integrated EELS intensity (I) from the Co and Ti $L_{2,3}$ edges as a function of depth (z) for the same sample shown in (a). In this plot z = 20 nm corresponds to the top surface of the NSCO, while the interface lies at $z \approx 11.5$ nm. In order to quantitatively parameterize the interface width, the Co and Ti profiles were fit to a simple Boltzmann-based sigmoidal function of the form $I_{Co/Ti} = 1 \pm [1 + \exp((z - z_0)/\Delta z)]$, where z_0 is the interface position and Δz provides a quantitative measure of the width. This results in Δz = 0.5 and 0.6 nm for Co and Ti respectively, i.e. 1-2 unit cells. Some beam broadening is expected due to dechanneling, meaning that this is an upper estimate of the interface width. Since the lattice parameters of both substrate and film are slightly below 0.4 nm the EELS profiles are consistent with a lack of major chemical interdiffusion and a sharp interface between STO and NSCO.

We begin our discussion of the magnetic and transport properties of these STO(001)/NSCO films with Fig. 5, which plots the temperature (T) dependence of the low field (H = 100 Oe) magnetization (M) and coercivity normalized to their 10 K values (top panel), electrical resistivity (ρ) in both zero and 90 kOe magnetic fields (middle panel), and the 90 kOe magnetoresistance (MR), defined as [ρ(H) - ρ(0) / ρ(0)] (bottom panel). The data are shown for three representative thicknesses; 620, 120 and 55 Å. Starting with $M(T)$ ($H_C(T)$ will be discussed below), we see from Fig 5(a) that the films exhibit bulk-like F properties at large thickness (i.e. 620 Å). The observed T_C is around 200 K, suppressed by about 20 K with respect to bulk polycrystals [36]. This is a similar magnitude of suppression with respect to bulk found in STO(001)/LSCO, which exhibits T_C values suppressed by 15-20 K at the same t [13,37]. Given the observation (Fig. 4) of an O vacancy superstructure it is obvious that at least some level of O deficiency must be present, despite the cool in O_2 and post-deposition anneal. It is worth pointing out that, based on the bulk phase diagram [36], an O deficiency of only 0.04, i.e. a chemical formula of $Nd_{0.5}Sr_{0.5}CoO_{2.96}$ would be sufficient to account for this reduction in T_C. Note that the lower F ordering temperatures for NSCO cf. LSCO (at any particular x value) are consistent with the narrower e_g-derived bandwidth expected from the reduced ionic size of Nd^{3+} (1.27 Å) cf. La^{3+} (1.36 Å). This results in a tolerance factor (TF) of about 0.970 (cf. 0.985 for LSCO [40]), which drives the observed symmetry change from rhombohedral (*R-3c*) / cubic (*Pm-3m*) [41] to orthorhombic (*Pnma*) [34,36,38] in bulk. The resultant decrease of Co-O-Co bond angle from 180 ° then leads to the reduced double exchange bandwidth, and T_C, in a simple picture. The other important feature present in $M(T)$ at t = 620 Å (Fig. 5(a)), is the clear decrease in M below about 60 K,

confirming that the ferrimagnetism induced by the antiferromagnetic ordering of the Nd^{3+} ions with respect to the Co sub-lattice [38] is preserved in thin films. The Nd ordering temperature (T_{ferri}) is 55-60 K, again slightly depressed in comparison to the 70 K bulk value [36,38]. As t decreases to 120 Å (Fig. 5(b)), and 55 Å (Fig. 5(c)) the qualitative form of $M(T)$ is unaltered but T_C and T_{ferri} decrease (see below for more details).

The transport and magnetotransport properties are shown as a function of t in the middle and lower panels of Fig. 5. At high t the $\rho(T)$ curve in $H = 0$ (Fig. 5(d)) reveals a 300 K resistivity around 3 mΩcm with negative $d\rho/dT$ over the entire measured temperature range. Application of $H = 90$ kOe leads to a negative MR which peaks at -4.5 % near 160 K, i.e. somewhat below T_C. As $T \rightarrow 0$ the MR decreases, falling to only -1 % at 5 K. The MR behavior at these high t values is thus rather similar to bulk, where the negative MR peaks just below T_C at values around -5.5 % [36]. However, the increased ρ in comparison to bulk (~ 0.3 mΩcm at 300 K for $x = 0.5$ [36]), and absence of a wide T interval over which a metallic-like T dependence (i.e. $d\rho/dT > 0$) is observed, is somewhat unexpected. In bulk polycrystalline samples positive $d\rho/dT$ emerges below T_C for $x \approx 0.30$ [36]. In the absence of additional data on the distortion of the CoO_6 octahedra in these strained thin films [42], we can only assume that effects such as increased O vacancy concentration (or other forms of increased disorder cf. bulk) are sufficient to induce a weakly semiconducting state in thin films. It should be noted that the lowering of the average A-site cation radius from $La_{0.5}Sr_{0.5}CoO_3$ (TF = 0.985) to $Pr_{0.5}Sr_{0.5}CoO_3$ (TF = 0.975) to $Nd_{0.5}Sr_{0.5}CoO_3$ (TF = 0.970) leads to a decrease in the residual resistivity ratio [$\rho(300\ K) / \rho_0$, where ρ_0 is the residual resistivity] of $x = 0.5$

polycrystalline bulk samples from 3 [14] to 1.7 [36]. It is thus clear that $Nd_{0.5}Sr_{0.5}CoO_3$ lies close to the boundary for the onset of localization of the electrons in the e_g-derived band. This is supported by observations on bulk $Pr_{1-x}Ca_xCoO_3$ at high x (TF ≈ 0.95), where a regime with $d\rho/dT > 0$ over a wide T interval does not occur [43]. In the context of the current study the behavior of $\rho(T)$ and MR(T) at lower thickness is of more interest. As shown in Fig. 5 (e), reducing t to 120 Å leads to only a small increase in ρ and a slightly stronger insulating-like T dependence. The peak in MR(T) below T_C is still present (Fig. 5(h)), although the low T tail in the MR is significantly more pronounced than in the 620 Å thick sample. At t = 55 Å (Fig. 5(f)) however, the increase in ρ is much more dramatic; the low T resistivity increases by over an order of magnitude in comparison to t = 120 Å, and a strongly insulating T dependence is observed, with no clear anomaly in $\rho(T)$ at T_C. A similarly dramatic change occurs in the MR (Fig. 5(i)). The small feature at T_C is now dominated by the large low T tail, the MR approaching -60 % at the lowest T measured. This greatly exceeds any MR observed in the long range ordered F metallic phase in bulk NSCO [36].

The t dependence of these magnetic and transport properties is summarized in Fig. 6, which plots T_C, T_{ferri}, the saturation magnetization (M_S, determined from 10 K $M(H)$ loops), and the MR at T = 35 K and H = 90 kOe. For purposes of comparison to bulk properties note that x = 0.5 bulk polycrystalline samples exhibit $T_C \approx 220$ K, $T_{ferri} \approx$ 70 K, $M_S \approx 0.8\ \mu_B$ / Co, and MR(T = 35 K) ≈ 0 [36]. The evidence for an abrupt crossover to a state below $t \approx 70$ Å with suppressed T_C, suppressed M_S, and enhanced resistivity and

low T MR is quite clear. The rapid increase in 35 K MR, from -6.5 % at t = 75 Å to -55 % at t = 55 Å is particularly dramatic. Importantly, as in the STO(001)/LSCO case [13,37], this low T MR exhibits all the characteristic signatures of the intercluster "GMR-type" effect discussed above [13,22], clearly distinguishing it from the more conventional MR effect found in the vicinity of T_C. Specifically, this low T MR is found to be negative, hysteretic (with peaks in ρ(H) at H_C), and isotropic with respect to the relative orientation of the injection current (I) and applied field. As an example, we find a 45 K negative MR of 37 % in 90 kOe with H perpendicular to I, compared to 36 % with H parallel to I (in both cases H is in-plane). As discussed above this form of MR can be definitively assigned to the situation where isolated nanoscopic F clusters exist in a non-F matrix [13,22]. In the case of STO(001)/LSCO this was further substantiated by direct detection of these nanoscopic magnetic clusters via SANS measurements on multiply-stacked films [13]. We thus conclude that below some thickness t* (70 Å in this case) an interfacial MEPS layer is found, explaining the existence of suppressed M_S, enhanced ρ, and an intercluster MR effect. The only quantitative difference in comparison to the STO(001)/LSCO system is the slightly smaller t* of 70 Å cf. 85 Å [13] (at x = 0.5). Given the extraordinary level of similarity with the case of STO(001)/LSCO we assume that this interfacial MEPS layer has the same microscopic origin, i.e. depth-wise variations in Sr and O concentration, which can be traced back to the differences between bulk and surface dopant dissolution energies, and tensile strain effects, respectively [13]. As in the STO(001)/LSCO case it is likely that the formation of O vacancies to accommodate lattice-mismatch with the substrate is important [13]. The formation of an O vacancy superstructure (Fig. 4) running perpendicular to the interface (as in

STO(001)/LSCO)) is thus significant. As a final comment on the data of Fig. 6 we should point out that $T_C(t)$ (which is discussed in more detail below) is in fact quantitatively similar in form to $T_{ferri}(t)$; when $T_C(t)/T_C(800\ \text{Å})$ is compared to $T_{ferri}(t)/T_{ferri}(800\ \text{Å})$ the curves are indistinguishable within the scatter of the data.

Having confirmed rapid degradation in electronic and magnetic properties below a thickness, t^*, of 70 Å, and having established that this is due to nanoscopic interfacial MEPS as in STO(001)/LSCO, 10 K $M(H)$ loops were measured at multiple t in order to determine whether $H_C(t)$ reflects the interfacial MEPS layer, as might be expected if this is intimately related to the anomalous H_C enhancement. The results, shown in Fig. 7, indeed provide clear evidence for the importance of the characteristic thickness t^*. The coercivity is found to increase gradually from 19.5 kOe at 800 Å to ~ 30 kOe near t^*. Below this H_C increases much more rapidly, reaching a plateau near 38 kOe in the region between 45 and 20 Å, before dropping precipitously to zero at even lower t. We therefore define three distinct regions (I, II, and III), as indicated on Fig. 7 and shown schematically in Figs. 8 (a-c). Region III ($t > t^*$) corresponds to the situation where a continuous long-range ordered F film with thickness (t - t^*) lies atop the magnetically inhomogeneous nanoscopic phase-separated layer of thickness t^*. Region II on the other hand ($t_{SP} \leq t \leq t^*$), corresponds to the situation where the entire film is composed of nanoscopic F clusters embedded in a non-F matrix. It will be shown below that these nanoscopic F clusters are single domain and, in this region, that they are thermally stable Finally, in region I ($t < t_{SP}$), as discussed in more detail below, the nanoscopic F clusters

become thermally unstable, i.e. superparamagnetism sets in, leading to the vanishing of H_C.

Measurements of $H_C(T)$ at various t provide considerable additional insight. Such data are shown in Fig. 5 (a-c), where the right axis shows $H_C(T)$ normalized to its low T value. Starting at t = 620 Å, i.e. deep into regime III of Fig. 7, we find that H_C decreases monotonically with T, falling smoothly to zero as $T \rightarrow T_C$. The form of $H_C(T)$ is in fact very similar to that seen in bulk NSCO [36] and LSCO [44] at x = 0.5, the superlinear T dependence being consistent with expectations for conventional Fs with strong irreversibility [44]. Fig. 5(b) shows that this behavior is preserved at t = 120 Å, i.e. a thinner film in region III. At t = 55 Å however (i.e. region II, $t < t^*$) very different behavior is observed. Specifically, H_C drops very quickly with increasing T, vanishing at 45 K, i.e. well below the point at which $M(T)$ measured in H = 100 Oe falls to zero. Measurements of $M(T)$ using a zero field cooling protocol (not shown) reveal a small peak at a similar temperature (48 K). These observations, particularly the absence of hysteresis above some value of T, clearly indicate the onset of superparamagnetism in this very thin film regime, with a blocking temperature, T_B, of 45 K at t = 55 Å. Quite simply, the isolated nanoscopic F clusters in the magnetically phase separated layer (Fig. 8(c)) become thermally unstable at very low t, leading to superparamagnetism. T_B thus marks a transition from a high T state where the cluster magnetizations fluctuate randomly on the time scale of the measurement, to a low T state where the individual cluster magnetizations freeze. It is worth noting that in the case of the t = 55 Å film T_B lies very close to T_{ferri}. It is thus possible that the ordering of the Nd lattice provides

additional magnetocrystalline anisotropy, thus contributing to the blocking transition. Low T measurements on an even thinner film (t = 12 Å), reveal that H_C vanishes at a lower blocking temperature of only 10 K.

Based on the above observations we can advance a simple qualitative picture capable of explaining all of the observed phenomena, particularly $H_C(t,T)$. After discussion of this qualitative picture we will present a simple quantitative analysis of the important magnetic parameters, demonstrating feasibility, and self-consistency, of the model. The basic picture is summarized schematically in Fig. 8. We propose that the nanoscopic short-range F clusters in the interfacial layer are single domain particles, and are elongated in the film growth direction. (For simplicity, we will model them as cylindrical.) This morphology is the simplest scenario consistent with the observed data, in particular the decrease in T_B with decreasing t, which necessarily requires that the single domain particles have volume that increases with t. Qualitatively, the H_C behavior observed in regions I, II and III can then be simply explained. Region III corresponds to a situation where the magnetization reverses via domain wall motion in the long-range ordered F overlayer. As $t \rightarrow t^{*+}$ the thickness of this uniform layer decreases, providing two obvious driving forces for the H_C enhancement with decreasing t; the influence of dimensional confinement on the motion of what are presumably Néel walls, and the domain wall pinning potential created by the inhomogeneous nanoscopic phase separated layer at the interface with the STO. We believe that both effects are likely active. The former is straight-forward and leads to an increase in H_C as $t \rightarrow t^{*+}$ due to the increased energy barrier associated with propagation of a Néel wall through a progressively thinner

uniform F film [45]. The second, i.e. the pinning of the domain walls [45,46] by the phase separated layer, is illustrated schematically in Figs. 8(d-f). In essence the total magnetic energy of the system is maximized when the domain walls in the long-range F overlayer align with the nanoscopic F clustered regions. Exact alignment of the domain wall with an F cluster would lead to the additional exchange energy cost associated with extending the domain wall through the F cluster to the interface with the STO(001) substrate. This is avoided (hence minimizing the total magnetic energy) by preferentially aligning the domain wall with the edge of the nanoscopic clusters or the non-F regions between the clusters, as shown in Fig. 8(d). Further motion of the domain wall then requires the additional input of energy required to switch the proximal F clusters, as shown in Fig. 8(e). The process is then repeated when the next F cluster is encountered (Fig. 8(f)). In essence the nanoscopic phase separated layer generates a quasiperiodic 2-D pinning potential for the long range F overlayer, producing a situation where the domain wall executes a "staggered" motion due to sequential pinning/depinning transitions. This leads to an enhancement of H_C, which increases strongly as $t \rightarrow t^{*+}$ (i.e. as the overlayer thickness approaches zero), as this is essentially an interface effect.

As t is further decreased to the point where it falls below t^* (i.e. the entry to region II, Fig. 8(b)) domain wall motion is no longer possible and the magnetization reversal in the single domain F clusters is forced to occur via rotation of the magnetization of the individual isolated clusters. In this region H_C is approximately constant (Fig. 7) until the cluster volume is reduced to the point where thermal stability of the nanoscopic cluster magnetization becomes an issue, i.e. the superparamagnetic

regime (region I). In this very thin film regime T_B decreases with decreasing t, reaching 45 K at t = 55 Å (Fig. 5(c)), before eventually falling below 10 K, leading to the vanishing H_C seen in Figure 7.

Simple quantitative estimates provide considerable support for this picture by demonstrating (a) that the scenario is feasible given the known magnetic properties of the material, and (b) that the model is self-consistent. The key magnetic parameters in the problem (e.g. the critical volume for superparamagnetism, the critical dimension for the single domain to multi-domain crossover, the domain wall width in the overlayer, etc.) require knowledge of M_S, the exchange stiffness (A), and the anisotropy constant (K). Given that we have detailed knowledge of M_S, and that A can be estimated from mean field theory, the central issue is the magnitude of K. The coercivity measured in region II provides a simple estimate of this magnetocrystalline anisotropy. Quite simply, we relate the maximum H_C value measured in region II (H_C^{max}) to the anisotropy constant using the Stoner-Wohlfarth expression [45] for coherent rotation of a single domain particle (the F clusters in this case):

$$K_U = \frac{M_S H_C^{\max}}{2} \qquad (1).$$

Note that we are explicitly assuming, for simplicity, that the magnetocrystalline anisotropy is uniaxial; K_U is the uniaxial anisotropy constant. Using 10 K values of M_S = 0.8 μ_B/Co and H_C^{max} = 38.5 kOe we obtain K_U = 2.5 x 10^6 erg/cm^3 for STO(001)/NSCO,

and similar values for STO(001)/LSCO. Although the available data are limited, the agreement with other literature values is very reasonable. Specifically, Aarbogh *et al* estimated the LSCO cluster anisotropy constant based on very simple arguments relating to the behavior of the bulk $M(T)$ and obtained $K_U \approx 0.3–1 \times 10^6$ erg/cm^3 [26]. The more accurate methods of Mira *et al* yielded $K_U = 2.1 \times 10^6$ erg/cm^3 at low T in $x = 0.3$ LSCO [47], in very good agreement with our value. This agreement is encouraging, and confirms that the single domain Stoner-Wohlfarth-like picture is indeed applicable to the nanoscopic F clusters.

Additional quantitative information can be garnered from the data on the superparamagnetic blocking temperature, T_B. Assuming, as is typical, an attempt frequency of order 10^9 Hz, the critical volume for the onset of thermal instability on a laboratory time scale of 1 s is given by [45],

$$V_{SP} = \frac{4}{3}\pi R_{SP}^3 = \frac{4}{3}\pi\left(\frac{6k_B T}{K_u}\right) \qquad (2).$$

It is clear from equation (2) that T_B scales with V_{SP}. Our data indicate $T_B = 45$ K at $t = 55$ Å and $T_B = 10$ K at $t = 12$ Å, meaning that the ratio of the blocking temperatures (4.5) scales almost exactly with the thickness ratios (4.6), strong evidence that the cross-sectional area of the F clusters is independent of t, i.e. the cylindrical geometry postulated above (Fig. 8(b,c)). Inserting $T_B = 45$ K and $K_u = 2.6 \times 10^6$ erg/cm^3 into (2), allows us to calculate the critical cluster radius for superparamagnetism (R_{clust}) from $V_{SP} = \pi R_{clust}^2 t$.

This generates a cluster radius of 20 Å, remarkably consistent with the direct (SANS-based) measurements of the cluster dimensions just under the percolation threshold (i.e. x = 0.18) in bulk LSCO (around 23 Å [23]). This demonstrates that the superparamagnetism we observe in the very thin film limit is consistent with the expected length scales for the magnetic phase separation effect in these systems. It is worth noting at this point that the dimensions of these nanoscopic F clusters lie far below the expected single domain to multi-domain crossover length scale, confirming that the assumption of single domain behavior is appropriate. In the large K_u limit (i.e. $K_U >> \mu_0 M_S^2$, easily satisfied in this case) the critical radius for the single domain to multi-domain crossover in a spherical particle is given by [45]:

$$R_{SD} = 9\frac{(AK_U)^{1/2}}{\mu_0 M_S^2} \qquad (3),$$

where μ_0 is the vacuum permeability. Making a simple mean field estimate of the exchange constant from T_C, the lattice coordination number (z) and the Co ion spin (S) [48], allows for estimation of A via $A \approx JS^2/d$, where d is the spacing between the Co ions. This gives A = 1 x 10^{-12} Jm^{-1}, which, when substituted into equation (3) yields R_{SD} in excess of 100 nm, i.e. much grater than the cluster dimensions. It is thus clear that the F nanoclusters in the magnetically phase separated interfacial layer are indeed expected to be single domain.

It is also worth pointing out that the expected domain wall widths in the F overlayer are on approximately the same scale as the size and spacing of the F clusters in

the interfacial MEPS layer. In the thin film limit (i.e. $t < \delta$) the Néel wall width is approximated by $\delta \approx \pi(A/K_U)^{1/2}$, which yields $\delta \approx 9$ nm, a value which is expected to decrease with increasing t [45]. This is very comparable to the F cluster diameter determined above (4 nm), and the cluster separation estimated from a simple comparison between the measured M_S at $t = t^*$ and the bulk M_S, which is of order 10 nm. These estimates confirm that the length scale describing the spatial variation of the 2D pinning potential are comparable to the expected domain wall widths, meaning that strong pinning effects are indeed possible.

As a final comment on the coercive properties of these STO(001)/NSCO epilayers it is worth pointing out that the nature of the magnetic anisotropy appears to be rather different than that seen in thin film manganites. Fig. 9 shows the 10 K in-plane angle (ϕ) dependence of H_C for a t = 800 Å sample, i.e. the thick film limit. Recall from Figs. 2 and 3 that these films remain significantly strained even at this thickness. Note that these data were simply extracted from anisotropic MR measurements of the type discussed in ref. 37. They thus provide only $H_C(\phi)$ rather than the remnance as a function of angle, which is more direct. Nevertheless, the data apparently reveal the overall symmetry of the magnetocrystalline anisotropy, which appears to take the form of two biaxial anisotropies phase shifted by 45°. Specifically, H_C reaches weak minima at 0, 90, 180, and 270°, in addition to stronger minima at 45, 135, 225, and 315°. The weak minima correspond to the <100> family of directions for the STO(001) substrate, whereas the strong minima correspond to the <110> family. The simplest interpretation of these data is that the films possess a biaxial anisotropy with the easy axes along the pseudocubic NSCO <110>

directions [49] (producing the minima at 45, 135, 225 and 315°), in addition to a second, substrate imposed, strain-induced biaxial anisotropy (producing the minima at 0, 90, 180, and 270°). The solid line through the data in Fig. 9 is in fact a simple model based on two biaxial anisotropies of differing magnitude. Although the existence of *minima* in $H_C(\phi)$ at the easy axes is at first sight counterintuitive, H_C being lower along the easy axis than the hard axis has in fact been observed before in manganite thin films [50], and, based on the form of $H_C(\phi)$ determined in prior work on manganite films [51], could even arise due to field misalignment. The essential difference between this situation and that seen in several prior studies on manganite films grown on STO is the existence of significant magnetocrystalline anisotropy intrinsic to the ferromagnet. In the manganite case the intrinsic anisotropy is so weak ($K \sim 10^4$ erg/cm^3 [52]) that the strain-induced [50], or surface step-induced [51] contributions dominate. In the much more highly anisotropic cobaltites ($K \sim 10^6$ erg/cm^3) the various contributions compete, the intrinsic anisotropy appearing to be largest. Although these inferences are somewhat speculative, they do demonstrate that future studies using torque magnetometry [52] and angle-dependent hysteresis loop measurements [50,51] would be well worthwhile. As in the manganite case it is likely that comparisons between (001) oriented and (110) oriented films will be needed to fully understand the behavior [50,52]. As a final remark on the data we note that future studies directed at understanding any possible relationship between the significant thin film magnetocrystalline anisotropies and the O vacancy ordering are also worthwhile.

IV. Summary and Conclusions

In summary, we have presented the results of a detailed study of the previously unexplained coercivity enhancement found to occur in thin film perovskite cobaltites grown on $SrTiO_3(001)$ substrates. The $SrTiO_3(001)/Nd_{0.5}Sr_{0.5}CoO_3$ system was chosen for this work and it was shown that it exhibits a rapid deterioration in magnetic and electronic properties below a thickness of approximately 70 Å, similar to $SrTiO_3(001)/La_{1-x}Sr_xCoO_3$. This deterioration is accompanied by the abrupt onset of large negative magnetoresistance at low temperatures, strong evidence that the degradation in magnetic and transport properties occurs due to interfacial magneto-electronic phase separation on a nanoscopic scale. Detailed temperature and thickness dependent measurements demonstrate that the observed coercivity enhancement is intimately related to this interfacial phase separation. The data are interpreted within a simple picture where the coercivity increase with decreasing thickness is driven by a combination of the finite size effect on Néel wall propagation in the continuous ferromagnetic overlayer, and the 2D pinning potential provided by the nanoscopic ferromagnetic cluster array. Simple quantitative estimates of the key parameters provide strong support for the model and demonstrate self-consistency.

Acknowledgements: Work at UMN supported primarily by NSF (DMR-0804432), with additional support from DoE (DE-FG02-06ER46275, specifically scattering characterization). Work at ORNL (MV) supported by the US DoE, Office of Basic Energy Sciences, Materials Sciences and Engineering Division. J.G. acknowledges the Spanish MEC 2007-0086 and the European Research Council Starting Investigator

Award. We are grateful to J.T. Luck for STEM specimen preparation and Andrew Baruth and Randall Victora for useful discussions.

References

1. See for example R. Ramesh and D.G. Schlom, MRS Bull. **33** 1006 (2008); J. Mannhart, D.H.A. Blank, H.Y. Hwang, A.J. Millis and J.-M. Triscone, MRS Bull. **33** 1027 (2008); E. Dagotto and Y. Tokura, MRS Bull. **33** 1037 (2008); N.A. Spaldin and R. Ramesh, MRS Bull. **33** 1047 (2008).

2. A. Gupta and J.Z. Sun, J. Mag. Mag. Mat. **200** 24 (1999).

3. M. Bowen, M. Bibes, A. Barthelemy, J.P. Contour, A. Anane, Y. Lemaitre and A. Fert, Appl. Phys. Lett. **82** 233 (2003).

4. J.-H. Park, E. Vescovo, H.-J. Kim, C. Kwon, R. Ramesh and T. Venkatesan, Phys. Rev. Lett. **81** 1953 (1998).

5. V. Garcia, M. Bibes, A. Barthelemy, M. Bowen, E. Jacquet, J.-P. Contour and A. Fert, Phys. Rev. B. **69** 052403 (2004).

6. J.J. Kavich, M.P. Warusawithana, J.W. Freeland, P. Ryan, X. Zhai, R.H. Kodama and J.N. Eckstein, Phys. Rev. B. **76** 014410 (2007).

7. F. Ott, M. Viret, R. Borges, R. Lyonnet, E. Jacquet, C. Fermon and J.-P. Contour, J. Mag. Mag. Mat. **211** 200 (2000).

8. A.X. Gray, C. Papp, B. Balke, S.-H. Yang, M. Hujiben, E. Rotenberg, A. Bostwick, S. Ueda, Y. Yamashita, K. Kobayashi, E.M. Gullikson, J.B. Kortright, F.M.F. de Groot, G. Rijnders, D.H.A. Blank, R. Ramesh and C.S. Fadley, Phys. Rev. B. **82** 205116 (2010).

9. M. Bibes, L. Balcells, S. Valencia, J. Fontcuberta, M. Wojcik, E. Jedryka and S. Nadolski, Phys. Rev. Lett. **87** 067210 (2001).

10. M. Hujiben, L.W. Martin, Y.-H. Chu, M.B. Holcomb, P. Yu, G. Rijnders, D.H.A. Blank and R. Ramesh, Phys. Rev. B. **78** 094413 (2008).

11. R.V. Chopdekar, E. Arenholz and Y. Suzuki, Phys. Rev. B. **79** 104417 (2009).

12. J.X. Ma, X.F. Liu, T. Lin, G.Y. Gao, J.P. Zhang, W.B. Wu, X.G. Li and J. Shi, Phys. Rev. B. **79** 174424 (2009).

13. M.A. Torija, M. Sharma, J. Gazquez, M. Varela, C. He, J. Schmitt, J.A. Borchers, M. Laver, S. El-Khatib and C. Leighton, Adv. Mater., in press (2011).

14. J. Wu and C. Leighton, Phys. Rev. B. **67** 174408 (2003).

15. L. Malavasi, E. Quartarone, C. Sanna, N. Lampis, A.G. Lehmann, C. Tealdi, M.C. Mozzati and G. Flor, Chem. Mater. **18** 5230 (2006).

16. C.H. Kim, G. Qi, K. Dahlberg, and W. Li, Science **327** 1624 (2010).

17. S. Madhukar, S. Aggarwal, A.M. Dhote, R. Ramesh, A. Krishnan, D. Keeble and E. Poindexter, J. Appl. Phys. **81** 3543 (1997).

18. E. Dagotto, *Nanoscale phase separation and colossal magnetoresistance*, Springer, New York (2002); E. Dagotto, T. Hotta and A. Moreo, Phys. Rep. **344** 1 (2001).

19. R. Caciuffo, D. Rinaldi, G. Barucca, J. Mira, J. Rivas, M.A. Senaris-Rodriguez, P.G. Radaelli, D. Fiorani and J.B. Goodenough, Phys. Rev. B. **59** 1068 (1999).

20. P.L. Kuhns, M.J.R. Hoch, W.G. Moulton, A.P. Reyes, J.Wu and C. Leighton, Phys. Rev. Lett. **91** 127202 (2003).

21. R.X. Smith, M.J.R. Hoch, P.L. Kuhns, W.G. Moulton, A.P. Reyes, G.S. Boebinger, J. Mitchell, and C. Leighton, Phys. Rev. B **78** 092201 (2008).

22. J. Wu, J.W. Lynn, C. Glinka, J. Burley, H. Zheng, J.F. Mitchell and C. Leighton, Phys. Rev. Lett. **94** 037201 (2005).

23. C. He, S. El-Khatib, J. Wu, J.W. Lynn, H. Zheng, J.F. Mitchell and C. Leighton, EPL **87** 27006 (2009).

24. D. Phelan, D. Louca, S. Rosenkranz, S.-H. Lee, Y. Qui, P.J. Chupas, R. Osborn, H. Zheng, J.F. Mitchell, J.R.D. Copley, J.L. Sarrao and Y. Moritomo, Phys. Rev. Lett. **96** 027201 (2006).

25. D. Phelan, D. Louca, K. Kamazawa, S.-H. Lee, S.N. Ancona, S. Rosenkranz, Y. Motome, M.F. Hundley, J.F. Mitchell and Y. Moritomo, Phys. Rev. Lett. **97** 235501 (2006).

26. H.M. Aarbogh, J. Wu, L. Wang, H. Zheng, J.F. Mitchell and C. Leighton, Phys. Rev. B. **74** 134408 (2006).

27. D. Fuchs, T. Schwarz, O. Moran, P. Schweiss and R. Schneider, Phys. Rev. B. **71** 092406 (2005).

28. C. Xie, J.I. Budnick, B.O. Wells and J.C. Woicik, Appl. Phys. Lett. **91** 172509 (2007).

29. B. Kundys and H. Szymczak, Phys. Stat. Sol. **201** 3247 (2004).

30. A.D. Rata, A. Herklotz, K. Nenkov, L. Schultz and K. Dorr, Phys. Rev. Lett. **100** 076401 (2008).

31. S.A. Baily and M.B. Salamon, J. Appl. Phys. **93** 8316 (2003).

32. A.Y. Samoilov, G. Beach, C.C. Fu, N.-C. Yeh and R.P. Vasquez, Phys. Rev. B. R14032 (1998).

33. A. Fondado, J. Mira, J. Rivas, C. Rey, M.P. Brejio and M.A. Senaris-Rodriguez, J. Appl. Phys. **87** 5612 (2000).

34. M. Paraskevopoulos, J. Hemberger, A. Krimmel and A. Loidl, Phys. Rev. B. **63** 224416 (2001).

35. R. Ganguly, A. Maignan, C. Martin, M. Hervieu and B. Raveau, J. Phys. Cond. Mat. **14** 8595 (2002).

36. D.D. Stauffer and C. Leighton, Phys. Rev. B. **70** 214414 (2004).

37. M.A. Torija, M. Sharma, M.R. Fitzsimmons, M. Varela, J. Wu and C. Leighton, J. Appl. Phys. **104** 023901 (2008).

38. A. Krimmel, M. Reehuis, M. Paraskevopoulos, J. Henberger and A. Loidl, Phys. Rev. B. **64** 224404 (2001).

39. See the following and references therein: J. Gazquez, W. Luo, M.P. Oxley, M. Prange, M.A. Torija, M. Sharma, C. Leighton, S.T. Pantelides, S.J. Pennycook, and M. Varela, Nano Lett., **11** 973 (2011)

40. For the purposes of this simple calculation high spin Co radii were used. The assumption of intermediate or low spin ions does not alter the overall argument.

41. LSCO is known to undergo a rhombohedral (*R-3c*) to cubic (*Pm-3m*) transition in this doping range.

42. S.J. May, J.-W. Kim, J.M. Rondinelli, E. Karapetrova, N.A. Spaldin, A. Bhattacharya and P.J. Ryan, Phys. Rev. B. **82** 014410 (2010).

43. S. Tsubouchi, T. Kyomen, M. Itoh and M. Oguni, Phys. Rev. B. **69** 144406 (2004).

44. H.P. Hunkel, R.M. Roshko, C. Viddal, L. Wei, G. Williams, X.Z. Zhou, J. Appl. Phys. **95** 7534 (2004).

45. R.C. O'Handley, *Modern Magnetic Materials: Principles and Applications*, Wiley, New York (2000).

46. H. Kronmuller and M. Fahnle, *Micromagnetism and the Microstructure of Ferromagnetic Solids*, Cambridge University Press, Cambridge (2003).

47. J. Mira, J. Rivas, M. Vazquez, M.R. Ibarra, R. Caciuffo and M.A. Senaris-Rodriguez, Europhys. Lett. **62** 433 (2003).

48. For simplicity, $S = 1$ was used in this simple estimate.

49. We are not aware of any work on magnetocrystalline anisotropy in bulk NSCO single crystals. Note that in the rhombohedral LSCO case the easy axes are known to be <111>. It is thus possible that the <110> easy axes we observe here are simply projections of the <111> on the (001) plane.

50. H. Boschker, M. Matthews, E.P. Houwman, H. Nishikawa, A. Vailionis, G. Koster, G. Rijnders and D.H.A. Blank, Phys. Rev. B. **79** 214425 (2009).

51. Z.-H. Wang, G. Cristiani and H.-U. Habermeier, Appl. Phys. Lett. **82** 3731 (2003).

52. Y. Suzuki, H.Y. Hwang, S.-W. Cheong, T. Siegrist, R.B. van Dover, A. Asamitsu and Y. Tokura, J. Appl. Phys. **83** 7064 (1998).

Figure Captions

Figure 1. Magnetization (normalized to the saturation value) as a function of applied magnetic field for (a) $Nd_{0.5}Sr_{0.5}CoO_3$, and (b) $La_{0.5}Sr_{0.5}CoO_3$ at 10 K. In both cases the data are shown for bulk polycrystals and 800 Å thick epitaxial films on $SrTiO_3(001)$.

Figure 2. High resolution wide-angle x-ray diffraction data on (a) a 420 Å thick $SrTiO_3(001)/Nd_{0.5}Sr_{0.5}CoO_3$ film, and (b) 45 – 800 Å thick films over an expanded angular range. The inset to (a) shows grazing incidence in-plane x-ray diffraction data (i.e. a ϕ scan) for a 800 Å thick film. The vertical dotted lines in (b) indicate the expected diffraction position for a fully relaxed film (left) and the observed diffraction position for films with in-plane lattice parameters matching the substrate (right).

Figure 3. Film thickness dependence of (a) the *c*-axis lattice parameter, (b) the full-width at half-maximum (FWHM) of the rocking curve through the (002) NSCO reflection, and (c) the length scale (Λ) extracted by applying the Scherrer formula to the wide angle diffraction peak width. The solid line line in (c) is the line $\Lambda = t$, and the dotted lines are guides to the eye. The vertical dotted line marks the critical thickness for strain relaxation.

Figure 4. *Z*-contrast STEM images of (a) a 90 Å thick $SrTiO_3(001)/Nd_{0.5}Sr_{0.5}CoO_3$ film at low magnification, (b) the interior of a 330 Å thick film showing the O vacancy superstructure, and (c,d) high resolution images of the substrate/film interface in the same film. An explicit scale bar is provided in (a); for (b)-(d) (atomic resolution images) note

the lattice parameters determined in the text. The inset to (b) is a fast Fourier transform of the image. Panel (e) shows a depth (z) profile of the normalized integrated EELS intensity for Co and Ti for the sample shown in (a). The dotted lines are fits to provide a simple characterization of the interface width, as described in the text.

Figure 5. Temperature dependence of the reduced magnetization (left axis) and coercivity (right axis) (top panel), resistivity in zero field and 90 kOe field (middle panel), and the magnetoresistance (bottom panel), defined as [ρ(90 kOe) - ρ(0) / ρ(0)]. The data are shown for film with thickness 620 Å (left panel), 120 Å (middle panel), and 55 Å (right panel).

Figure 6. Thickness dependence of (a) the Curie and ferrimagnetic ordering temperatures, (b) the 10 K saturation magnetization, and (c) the 35 K 90kOe magnetoresistance. Note the log scale in (c). The vertical dotted line marks the characteristic thickness, t^*. Other dotted lines are guides to the eye.

Figure 7. Thickness dependence of the 10 K coercivity. The data are divided into three thickness regions by the characteristic thicknesses t^* and t_{SP}, marked by the vertical dotted lines. The dotted line through the data is a guide to the eye.

Figure 8. (a-c): Schematic representations of the magnetic structure of films in regions III, II and I respectively. The dark regions are ferromagnetically ordered. (d-f): Schematic

representations of the magnetic structure of a film in region III as a Néel wall propagates through the ferromagnetic overlayer.

Figure 9. Polar plot of the angle dependence (in degrees) of the coercivity for an 800 Å thick film at 10 K. The field is applied in the plane of the film. The dotted arrows show the in-plane <100> family of directions for the STO(001) substrate. The solid arrows show the <110> family of directions (pseudocubic) for the NSCO. The solid line through the data is a simple fit to two phase-shifted biaxial anisotropies of different magnitude, as discussed in the text.

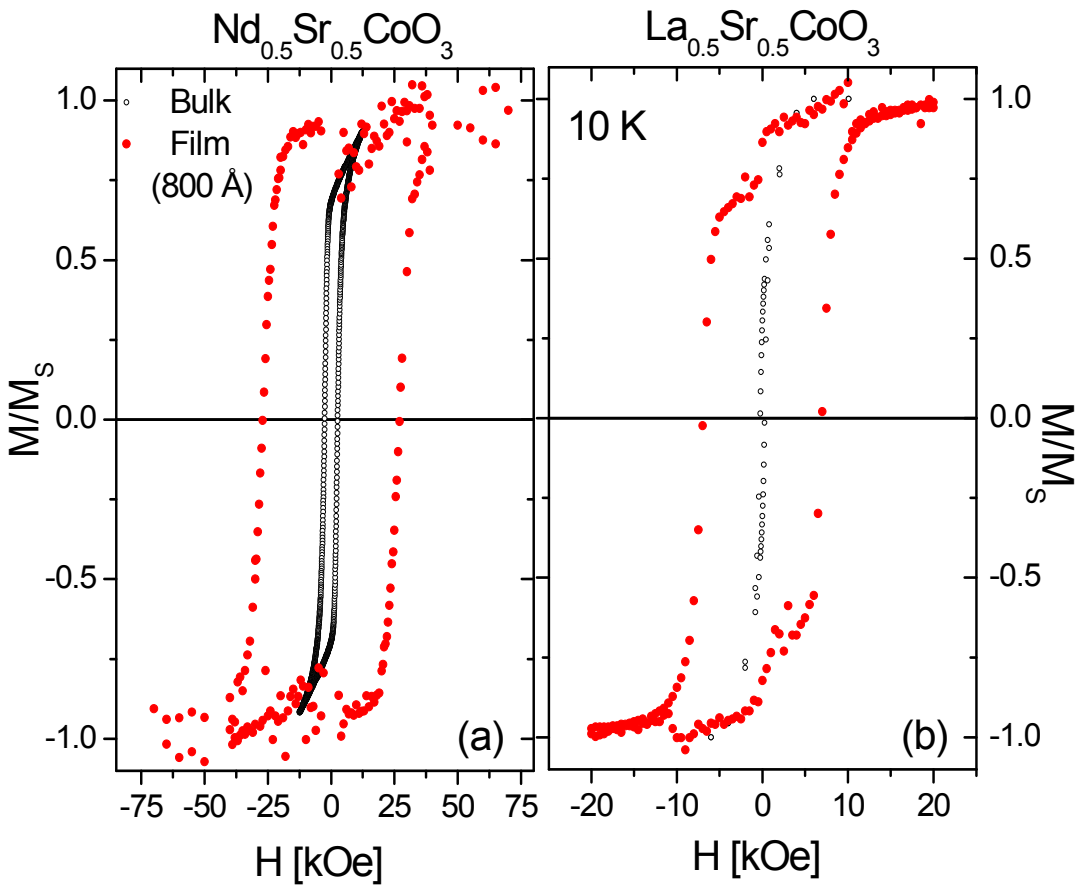
Nd0.5Sr0.5CoO3
La0.5Sr0.5CoO3
Bulk
Film
(800 Å)
10 K
(a)
(b)
M/Ms
H [kOe]
1.0
0.5
0.0
-0.5
-1.0
-75
-50
-25
0
25
50
75
-20
-10
0
10
20

Figure 1

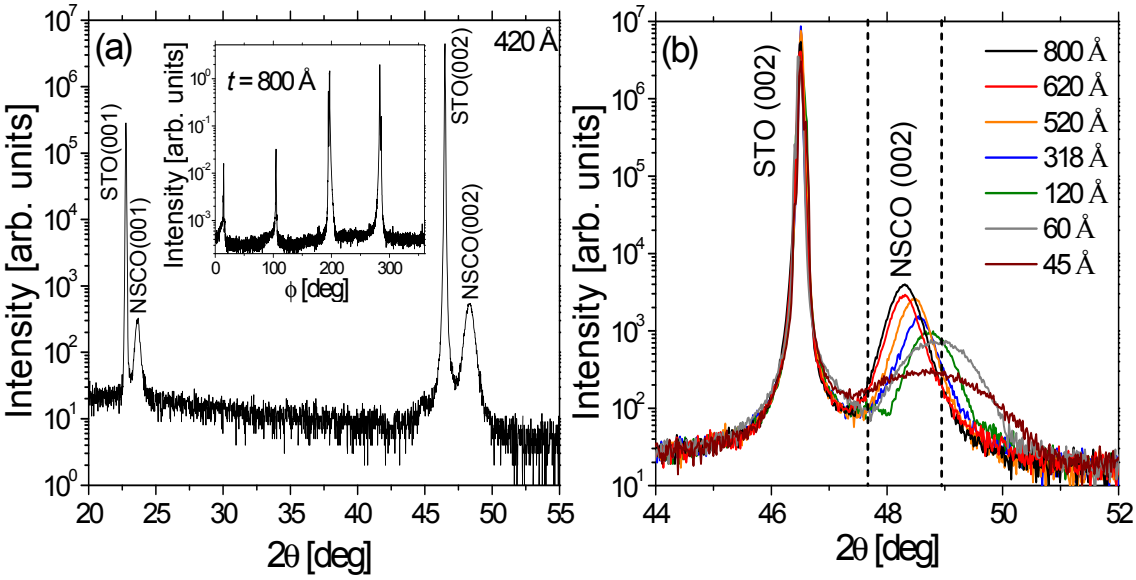
(a)
420 Å
STO(001)
NSCO(001)
STO(002)
NSCO(002)
Intensity [arb. units]
2θ [deg]
t = 800 Å
Intensity [arb. units]
ϕ [deg]
(b)
STO (002)
NSCO (002)
800 Å
620 Å
520 Å
318 Å
120 Å
60 Å
45 Å
Intensity [arb. units]
2θ [deg]

Figure 2

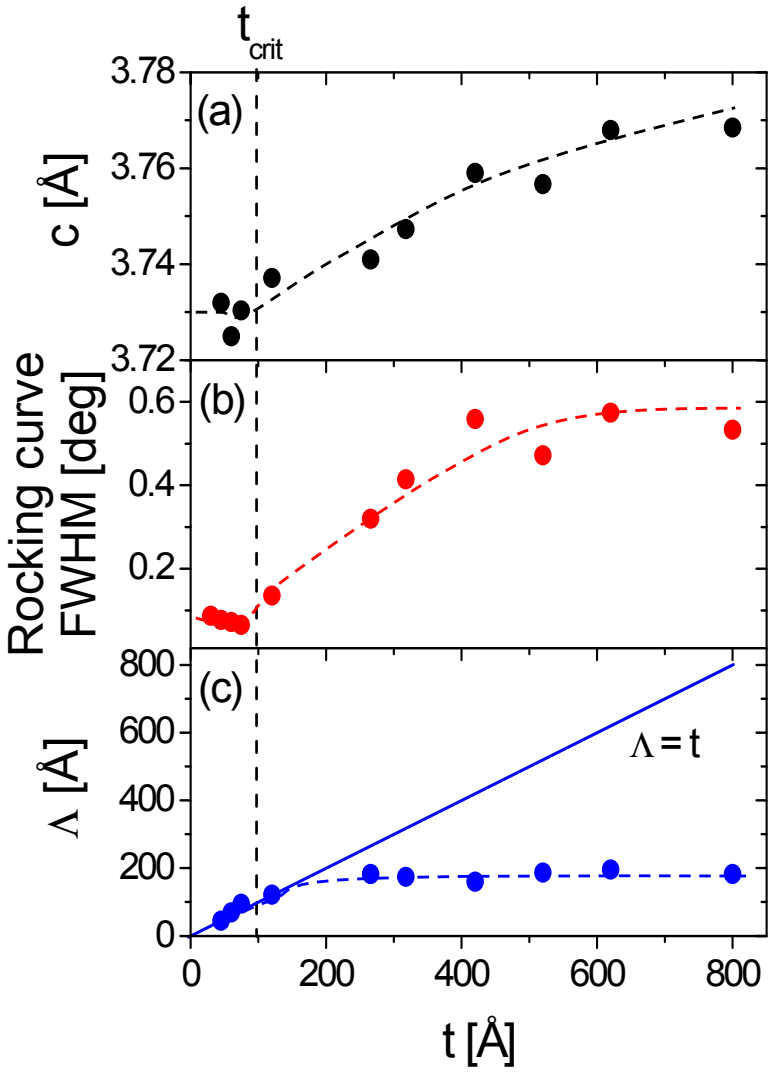
t crit
3.78
3.76
3.74
3.72
(a)
c [Å]
0.6
0.4
0.2
(b)
Rocking curve
FWHM [deg]
800
600
400
200
0
(c)
Λ [Å]
Λ = t
0
200
400
600
800
t [Å]

Figure 3

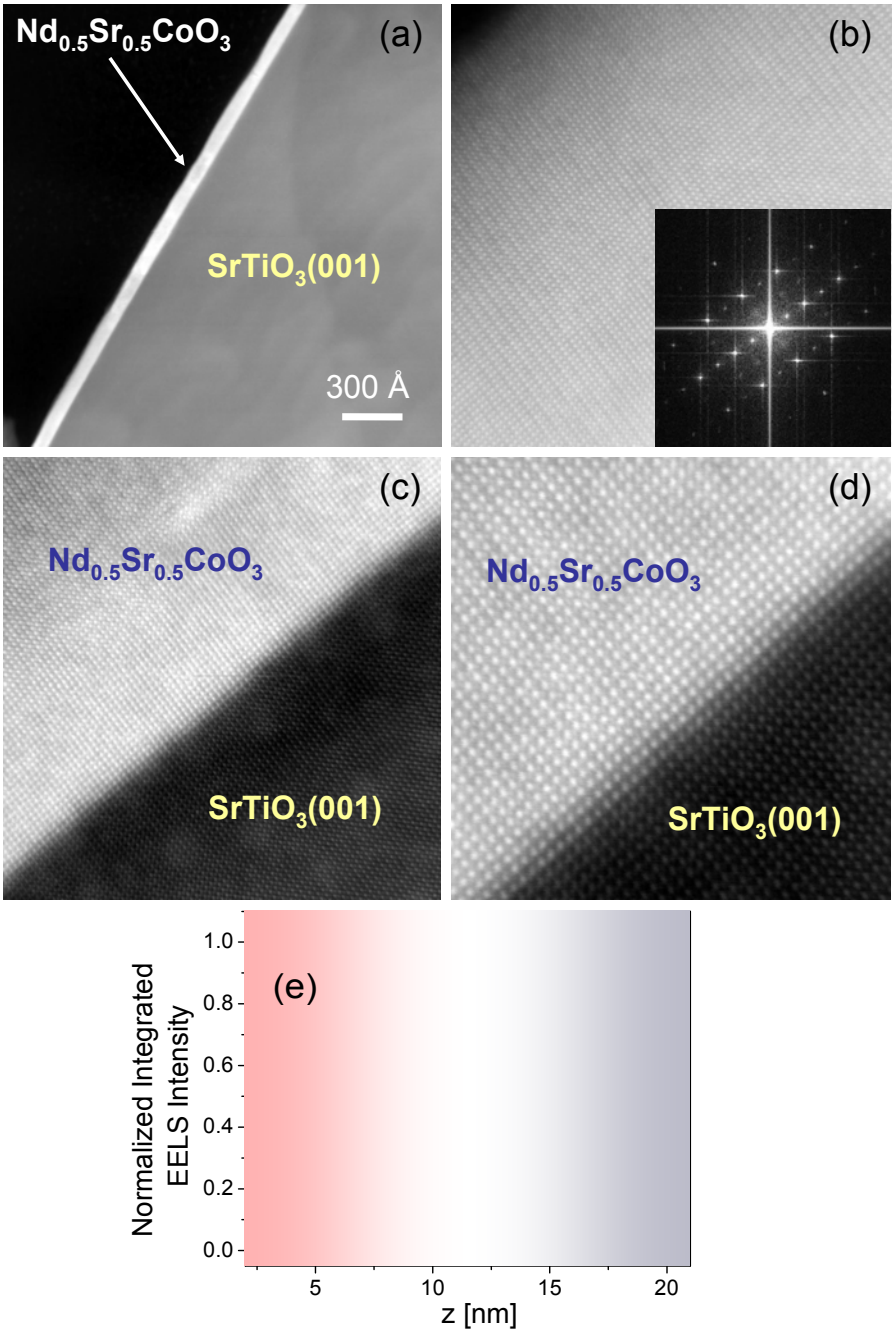
Nd0.5Sr0.5CoO3
(a)
SrTiO3(001)
300 Å
(b)
(c)
Nd0.5Sr0.5CoO3
SrTiO3(001)
(d)
Nd0.5Sr0.5CoO3
SrTiO3(001)
(e)
Normalized Integrated EELS Intensity
1.0
0.8
0.6
0.4
0.2
0.0
5
10
15
20
z [nm]

Figure 4

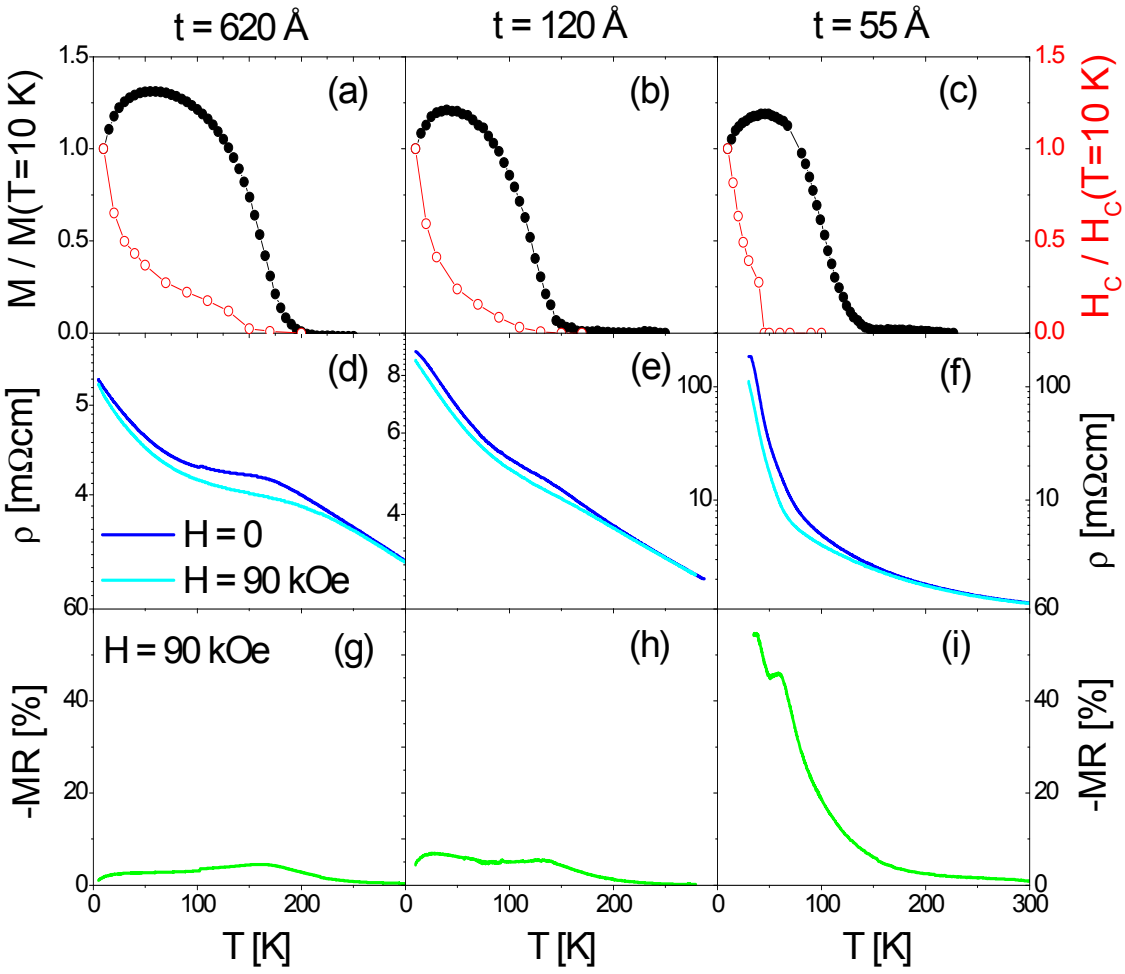
t = 620 Å
t = 120 Å
t = 55 Å
(a)
(b)
(c)
(d)
(e)
(f)
(g)
(h)
(i)
M / M(T=10 K)
H_C / H_C(T=10 K)
ρ [mΩcm]
-MR [%]
H = 0
H = 90 kOe
H = 90 kOe
T [K]
T [K]
T [K]

Figure 5

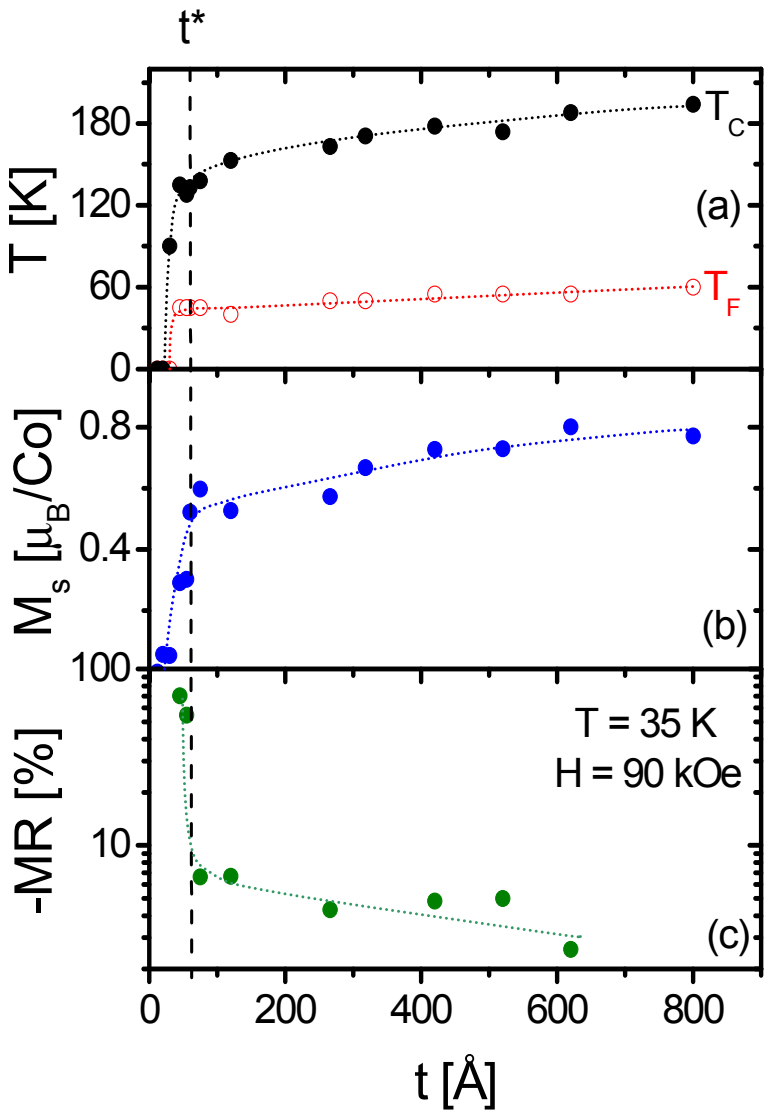
t*
T [K]
180
120
60
0
T_C
(a)
T_F
M_s [μ_B/Co]
0.8
0.4
(b)
-MR [%]
100
10
T = 35 K
H = 90 kOe
(c)
0
200
400
600
800
t [Å]

Figure 6

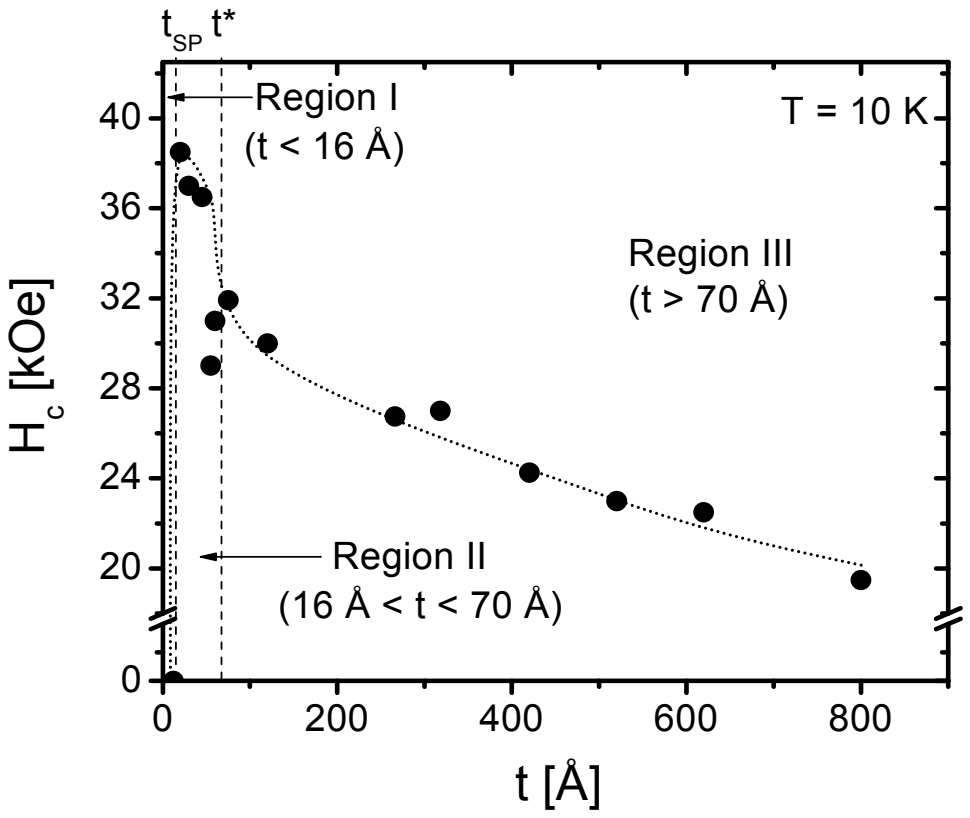
t_SP t*
Region I
(t < 16 Å)
T = 10 K
Region III
(t > 70 Å)
Region II
(16 Å < t < 70 Å)
H_c [kOe]
t [Å]
0
20
24
28
32
36
40
0
200
400
600
800

Figure 7

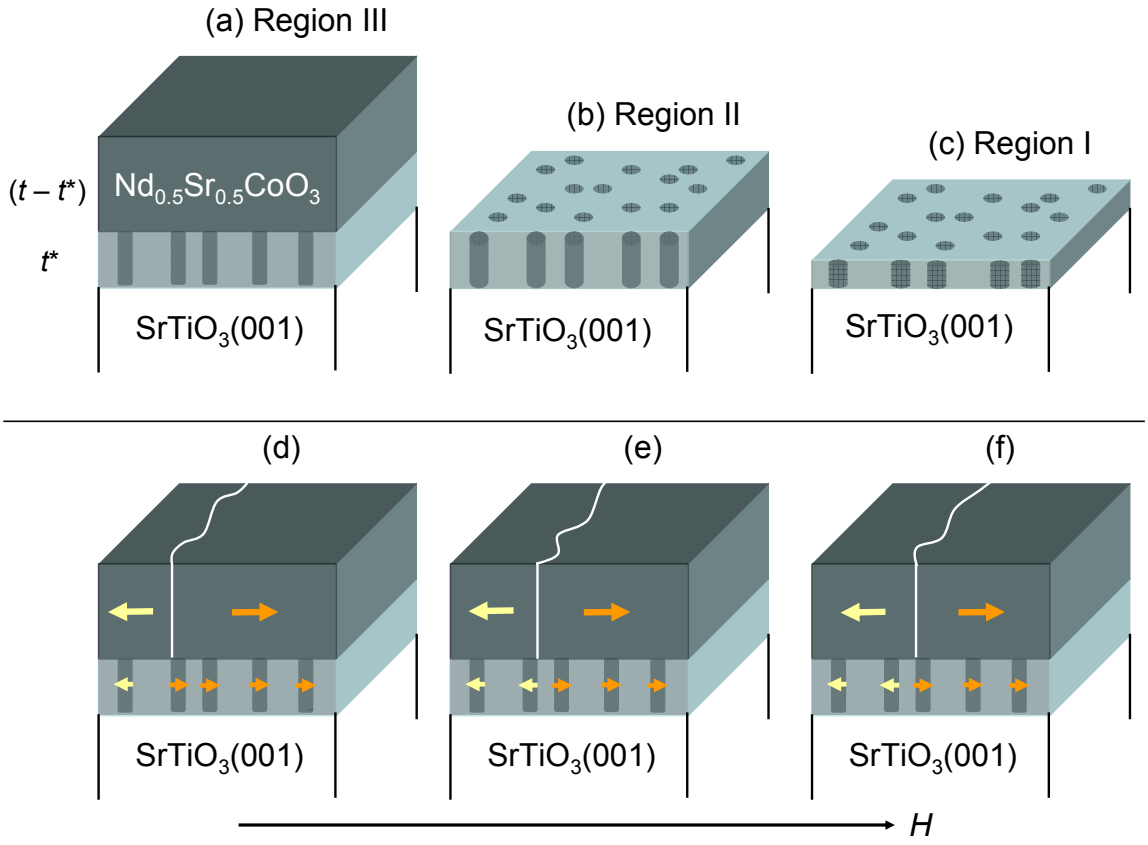
(a) Region III
(b) Region II
(c) Region I
(t – t*)
t*
Nd0.5Sr0.5CoO3
SrTiO3(001)
SrTiO3(001)
SrTiO3(001)
(d)
(e)
(f)
SrTiO3(001)
SrTiO3(001)
SrTiO3(001)
H

Figure 8

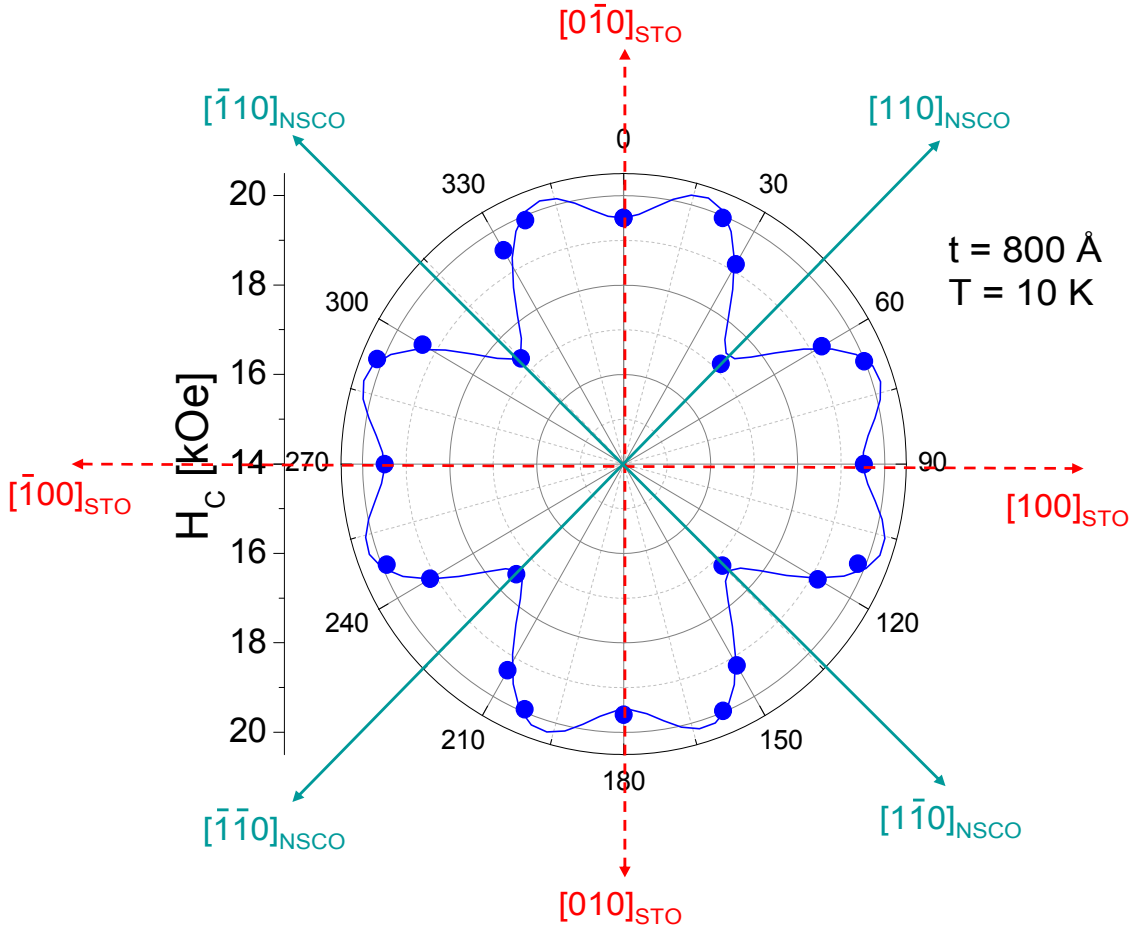
[0$\bar{1}$0]$_{STO}$
[$\bar{1}$10]$_{NSCO}$
[110]$_{NSCO}$
0
30
60
90
120
150
180
210
240
270
300
330
20
18
16
14
16
18
20
H$_c$ [kOe]
t = 800 Å
T = 10 K
[$\bar{1}$00]$_{STO}$
[100]$_{STO}$
[$\bar{1}\bar{1}$0]$_{NSCO}$
[1$\bar{1}$0]$_{NSCO}$
[010]$_{STO}$

Figure 9